JACS
JOURNAL OF THE AMERICAN CHEMICAL SOCIETY
Article
pubs.acs.org/JACS

Solution Growth of Single Crystal Methylammonium Lead Halide Perovskite Nanostructures for Optoelectronic and Photovoltaic Applications

Yongping Fu, Fei Meng, Matthew B. Rowley, Blaise J. Thompson, Melinda J. Shearer, Dewei Ma, Robert J. Hamers, John C. Wright, and Song Jin*

Department of Chemistry, University of Wisconsin-Madison, 1101 University Avenue, Madison, Wisconsin 53706, United States

Supporting Information

ABSTRACT: Understanding crystal growth and improving material quality is important for improving semiconductors for electronic, optoelectronic, and photovoltaic applications. Amidst the surging interest in solar cells based on hybrid organic–inorganic lead halide perovskites and the exciting progress in device performance, improved understanding and better control of the crystal growth of these perovskites could further boost their optoelectronic and photovoltaic performance. Here, we report new insights on the crystal growth of the perovskite materials, especially crystalline nanostructures. Specifically, single crystal nanowires, nanorods, and nanoplates of methylammonium lead halide perovskites ($CH_3NH_3PbI_3$ and $CH_3NH_3PbBr_3$) are successfully grown via a dissolution-recrystallization pathway in a solution synthesis from lead iodide (or lead acetate) films coated on substrates. These single crystal nanostructures display strong room-temperature photoluminescence and long carrier lifetime. We also report that a solid–liquid interfacial conversion reaction can create a highly crystalline, nanostructured $MAPbI_3$ film with micrometer grain size and high surface coverage that enables photovoltaic devices with a power conversion efficiency of 10.6%. These results suggest that single-crystal perovskite nanostructures provide improved photophysical properties that are important for fundamental studies and future applications in nanoscale optoelectronic and photonic devices.

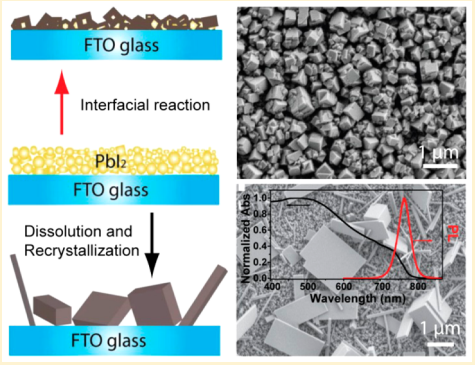

INTRODUCTION

Methylammonium lead iodide perovskite, $CH_3NH_3PbI_3$ ($MAPbI_3$), is emerging as a "superstar" semiconductor for cost-effective photovoltaic (PV) applications.[1−4] It is a semiconductor with a suitable and direct optical band gap (1.57 eV), a high optical absorption coefficient ($\alpha = 10^4$–10^5 cm^{-1} for $h\nu > 1.7$ eV), and a long electron/hole diffusion length (a few μm) even in solution-processed polycrystalline thin films, making $MAPbI_3$ advantageous in both photovoltaic and other optoelectronic applications.[5−10] Recent work reports a solar conversion efficiency of 19.3%, a value that surpasses dye-sensitized, quantum dot, organic and amorphous silicon solar cells, and other emerging PV technologies.[11,12] Due to these excellent attributes and the ease of processing, low cost, and earth abundance, if the stability and toxicity concerns can be addressed, perovskite solar cells could potentially become the next-generation commercial PV technology.[13]

Up to now, a variety of methods have been successfully used to prepare $MAPbI_3$ thin films for photovoltaic devices, including spin-coating from a $MAPbI_3$ solution,[2,14] sequential solution deposition,[3,15] vapor coevaporation,[4,16] and vapor-assisted solution conversion.[17] These techniques usually produce polycrystalline $MAPbI_3$ perovskite thin films. Despite the excellent photovoltaic performance achieved with such polycrystalline films, conventional solar cell research shows that the lower impurity and defect concentration in high-quality single crystal semiconductors leads to better device performance over polycrystalline films. Moreover, fewer scattering crystal boundaries could also improve charge transport.[18] Very recently, research has shown that improving the quality of crystals or passivating their surface could further improve device efficiency.[19−22] In addition, large lead halide perovskite single crystals have also been grown using a top-seeded-solution-growth method or an antisolvent vapor-assisted crystallization process, and optical and transport characterization revealed exceptional low traps density and a charge carrier diffusion length exceeding tens of μm in these single crystals.[23,24] Therefore, understanding and improving the crystal growth of lead halide perovskites[25−27] would benefit the fundamental studies and further enhance their applications.

Moreover, there have been a number of studies on single crystalline semiconductor nanostructures such as one-dimensional (1D) nanowires and two-dimensional (2D) nanoplates that have superior optical and electrical properties to their bulk counterparts.[28,29] These structures are promising candidates for

Received: March 13, 2015
Published: April 14, 2015

ACS Publications © 2015 American Chemical Society

DOI: 10.1021/jacs.5b02651
J. Am. Chem. Soc. 2015, 137, 5810−5818

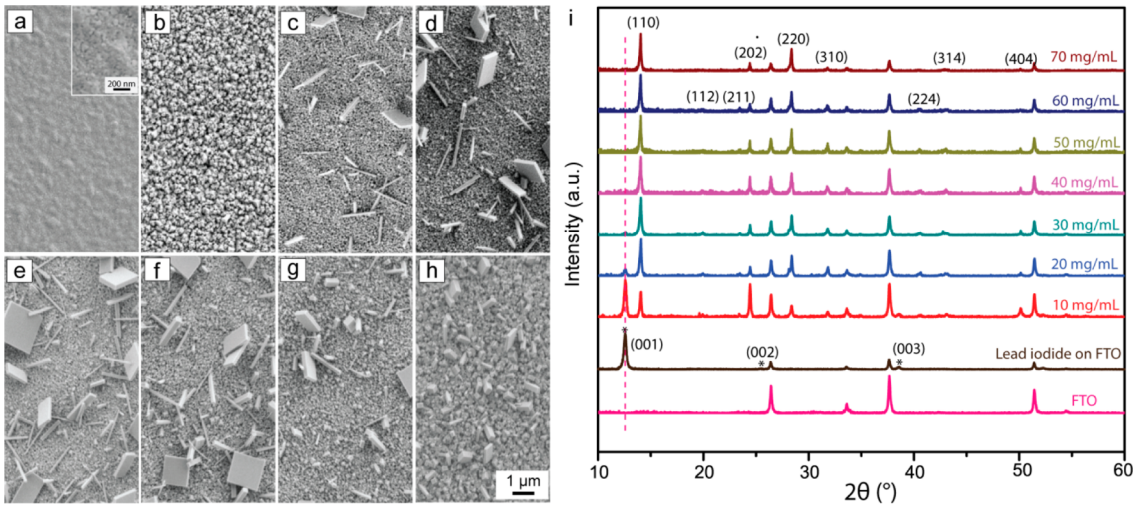

Figure 1. Morphologies and PXRD patterns of as-grown $MAPbI_3$ nanostructures using PbI_2 and different concentrations of MAI/IPA solutions at a reaction time of 10 min. (a) Scanning electron microscope (SEM) images of predeposited PbI_2 film on FTO substrate. (b–h) SEM images of as-grown $MAPbI_3$ nanostructures grown using conditions of 10, 20, 30, 40, 50, 60, and 70 mg/mL of MAI/IPA solution, respectively. All the images share the same scale bar shown in (h). (i) PXRD patterns of $MAPbI_3$ nanostructures grown at different MAI concentrations, in comparison with lead iodide and FTO substrate.

nanoelectronic, nanophotonic, and photovoltaic applications.[30−35] These nanoscale building blocks are also used in both fundamental studies and as proof-of-principle studies of solar device design and improvement.[33,36−39] With the exception of *polycrystalline* $MAPbI_3$ nanoplatelets and nanowires[40−44] and small single crystalline nanocrystals,[45] there have been no reports of 1D or 2D nanostructures of single crystal lead halide perovskites ($MAPbI_3$ or $MAPbBr_3$) that are suitable as nanoscale building blocks for nanoelectronic, nanophotonic, and photovoltaic applications.

In this article, we first report mechanistic insights on the crystal growth of lead halide perovskite nanostructures using a facile solution conversion from lead iodide (and lead acetate) films to $MAPbI_3$ and $MAPbBr_3$. Despite the widespread use of such a conversion process for solar device fabrication, the underlying conversion mechanism was not well understood.[46] Here, we show that the $MAPbI_3$ conversion growth involves two possible pathways, an interfacial reaction process or a dissolution-recrystallization process, whose relative importance depends on the MAI precursor concentration. Following the dissolution-recrystallization growth mechanism, single crystal nanowires (NWs), nanorods (NRs), nanobelts (NBs), and nanoplates of $MAPbI_3$ are successfully grown. The room-temperature photoluminescence (PL) intensity of these 1D and 2D perovskite nanostructures is 200 times stronger than bulk single crystals directly grown from aqueous solutions, and the carrier lifetime is ∼10 times longer. In addition, following the interfacial reaction mechanism, we have created a highly crystalline nanostructured $MAPbI_3$ film with micrometer grain size and high surface coverage. Preliminary fabrication of photovoltaic devices based on such films achieved a power conversion efficiency of 10.6%. These results suggest high-quality single-crystal perovskite materials can be a better choice for fundamental studies of the physical properties and the photovoltaic and optoelectronic applications of perovskites.

RESULTS AND DISCUSSION

Growth and Characterizations of Single Crystal $MAPbI_3$ Nanostructures. To synthesize single crystal perovskite NWs, NRs, and nanoplates, a compact and uniform lead iodide (PbI_2) film was first introduced on fluorine-doped tin oxide (FTO) substrates by spin-coating PbI_2 solution in dimethylformamide (DMF) and then dipping it into methylammonium iodide (CH_3NH_3I, MAI) solution in isopropanol (IPA) (see details in the Experimental Section). Figure 1a shows the morphology of PbI_2 film before conversion. It exhibits uniform grains of several tens of nanometers. The PbI_2 deposited by spin-coating from DMF solution is the hexagonal 2H polytype, as confirmed by powder X-ray diffraction (PXRD), where the four diffraction peaks correspond to the (001), (002), (003), and (004) lattice planes of PbI_2 (see Figure 1i, black curve).[3]

We first investigated the effect of MAI concentration on crystal growth at room temperature, while the growth time was fixed at 10 min. Representative morphologies of as-converted films using different concentrations of MAI are shown in Figure 1b–h. The corresponding powder X-ray diffraction (PXRD) patterns are provided in Figure 1i. The film converted at an MAI concentration of 10 mg/mL exhibits many crystalline cubic-like grains with a size of several tens of nanometers on top of the surface. However, the PXRD (Figure 1i, red curve) shows both the diffraction peaks from the $MAPbI_3$ phase and a relatively strong diffraction peak at 12.60° that corresponds to the (001) lattice plane of unconverted PbI_2, indicating the conversion is incomplete. The reason for incomplete conversion may be that the crystalline $MAPbI_3$ initially formed on the surface obstructs the continual diffusion of MA^+ ions to react with PbI_2, which will be discussed later. However, it is interesting that increasing the concentration of MAI (i.e., 20–60 mg/mL) leads to the growth of perovskite NRs and nanoplates with well-defined facets (Figure 1c–g). It is noteworthy that this concentration regime has rarely been explored in previously reported synthesis of $MAPbI_3$ thin films. However, when the concentration of MAI was further increased above 70 mg/mL, the NRs and nanoplates were reduced in both size and density again (Figure 1h). Dissolution of PbI_2 was also observed. We note the FTO substrates are almost covered by $MAPbI_3$ nanoparticles in Figure 1c–h. The PXRD (Figure

DOI: 10.1021/jacs.5b02651
J. Am. Chem. Soc. 2015, 137, 5810−5818

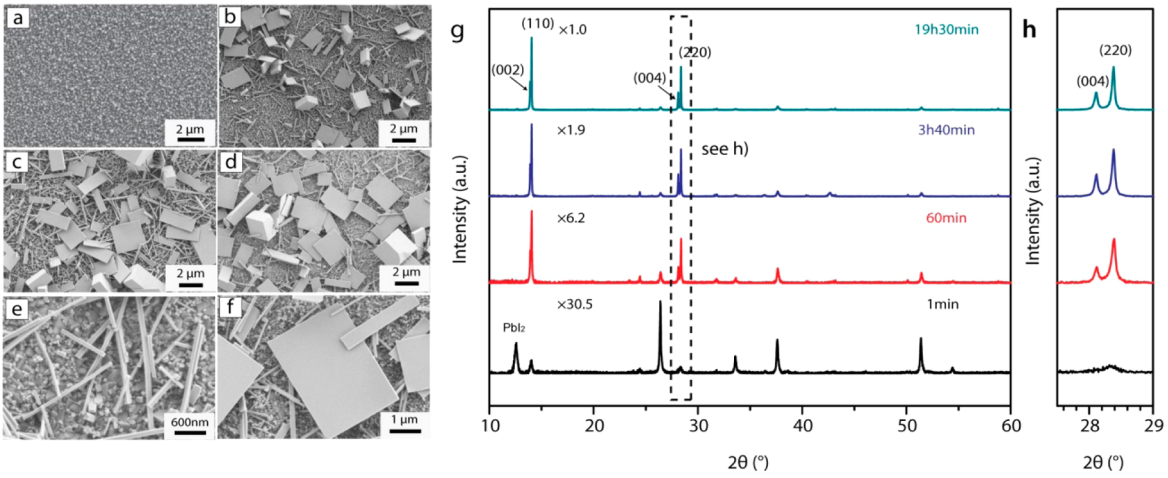

Figure 2. Structural characterizations of $MAPbI_3$ nanostructures synthesized using PbI_2 precursor at different reaction times. The concentration of MAI/IPA solution is fixed at 40 mg/mL. (a–d) SEM images of as-grown $MAPbI_3$ perovskite nanostructures at a reaction time of 1 min, 60 min, 3 h 40 min, and 19 h 30 min. (e and f) More SEM images with higher magnification of as-grown perovskite nanostructures at the 19 h 30 min reaction time. (g) Corresponding PXRD patterns. To compare relative diffraction intensity, all peak intensities are normalized to the strongest (110) diffraction peak of the $MAPbI_3$ film grown at 19 h 30 min. (h) Details for the dashed rectangular box in (g).

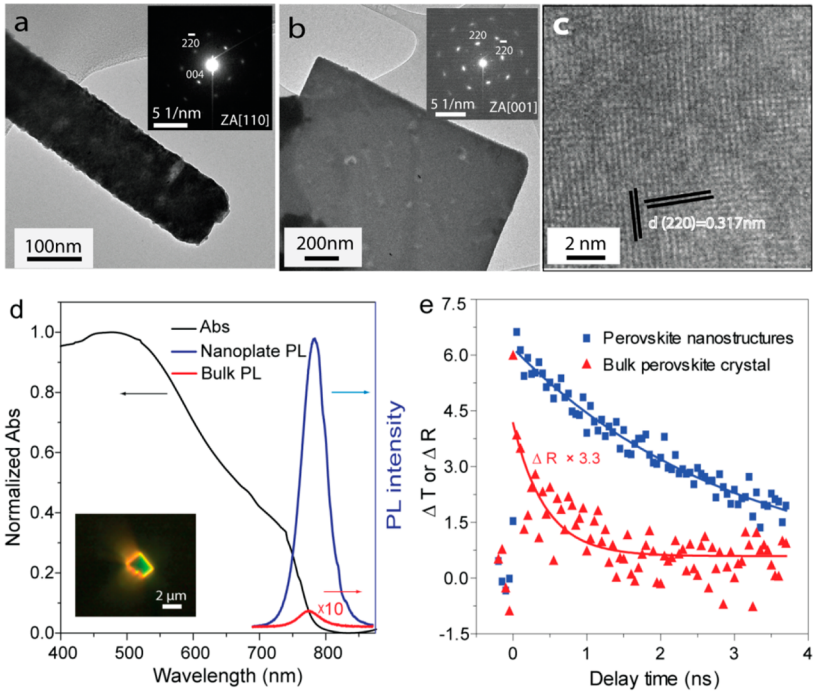

Figure 3. Transmission electron microscope (TEM) characterizations of single crystal $MAPbI_3$ NW and nanoplate and optical characterizations of single crystal $MAPbI_3$ nanostructures and bulk crystal. (a) Low-resolution TEM image of a $MAPbI_3$ NW; inset is the corresponding SAED pattern along ZA [110]. (b) Low-resolution TEM image of a $MAPbI_3$ nanoplate; inset is the corresponding SAED pattern along ZA [001]. (c) High-resolution TEM image of a single crystal $MAPbI_3$ nanoplate. (d) Visible absorption spectrum of $MAPbI_3$ film synthesized from a 40 mg/mL MAI/IPA solution and 30 min reaction time (black curve) in comparison with the confocal microscopy photoluminescence of a single nanoplate (blue curve) and bulk crystal (red curve) excited by a 532 nm laser source, respectively. The inset shows a dark-field optical microscopy image of a single $MAPbI_3$ nanoplate with a size of about 2 μm × 3 μm. (e) Carrier decay dynamics of $MAPbI_3$ perovskite nanostructures (transmission mode) and bulk single crystal (reflection mode) at 795 nm under a pump fluence of 9.8 $\mu J/cm^2$.

1i) confirms the as-converted $MAPbI_3$ is the tetragonal perovskite phase (space group *I4/mcm*, a = 8.8743 Å, c = 12.6708 Å) at all MAI concentrations, while some amounts of PbI_2 still exist at low MAI concentrations (i.e., 10 and 20 mg/mL). However, the (001) diffraction peak from PbI_2 gradually disappears as MAI concentration increases, indicating the conversion is faster and more complete.

The effect of reaction time on crystal growth was then investigated. The experiments were carried out at room temperature under the same concentration of MAI at 40 mg/mL. Parts a–d of Figure 2 display the SEM images of as-grown $MAPbI_3$ perovskite at a reaction time of 1 min, 60 min, 3 h 40 min, and 19 h 30 min, respectively. At a growth time of 1 min, the morphology of as-converted $MAPbI_3$ is similar to Figure 1b, exhibiting many crystalline cubic-like grains with flat facets. At

DOI: 10.1021/jacs.5b02651
J. Am. Chem. Soc. 2015, 137, 5810–5818

10 min, we can clearly see NWs and nanoplates have grown from the surface (Figure 1e). The size of these $MAPbI_3$ nanostructures continues to increase as the reaction time increases further. In addition, we notice that in the background the $MAPbI_3$ perovskite nanoparticles on FTO progressively dissolved. The products at 19 h 30 min are NWs, NRs, and nanoplates with well-defined flat facets on almost bare FTO substrates, as highlighted in Figure 2e and f. The NRs ranges from 1 to 3 μm in length and are several tens of nanometers in diameter. The size and shape of the nanoplates vary, while the thickness is usually around a few hundred nanometers. Figure 1f shows a nanoplate with ~2.3 μm × 3 μm dimensions and a nanobelt with ~0.5 μm × 2.5 μm dimensions. The PXRD patterns of the $MAPbI_3$ nanostructures (Figure 1g) show that the diffraction peak intensity increases dramatically as the reaction time increases, indicating a significant enhancement in the crystallinity of $MAPbI_3$ nanostructures. By fitting the PXRD patterns, we can obtain unit cell parameters of a = 0.8884 nm and c = 12.690 nm, in agreement with previous results.[46−48] Moreover, the clear split of the (220) and (004) peaks (highlighted in Figure 2h) further confirms that the as-grown $MAPbI_3$ nanostructures are the tetragonal phase and have high crystal quality.[47,49] The appearance of (002) and (004) peaks as reaction time increases may also suggest the $MAPbI_3$ nanoplates preferentially orientate along the (001) direction.

The transmission electron microscope (TEM) and electron diffraction (ED) analysis of the $MAPbI_3$ nanostructures further confirms the crystal structure and single crystal nature of the products (Figure 3a−c). Representative low-resolution TEM images (Figure 3a, b) of some representative NWs and nanoplates obtained under 120 kV electron beam confirm the product is single crystalline. The sharp diffraction spots seen in the corresponding selected area electron diffraction (SAED) patterns shown in the insets can be indexed to a tetragonal perovskite crystal structure with the zone axes (ZAs) of [110] or [001]. It is clear that the large flat facets of the $MAPbI_3$ nanoplates are the c planes of the tetragonal perovskite crystal structure. The acquisition of high-resolution TEM on NWs is challenging, due to instability of NWs under 200 kV electron beam. Nevertheless, the nanoplates appear slightly more stable than NWs, likely due to their larger size. The stability allowed us to obtain lattice-resolved high-resolution TEM (HRTEM) images. A representative HRTEM image of a $MAPbI_3$ nanoplate (Figure 3c) shows an interplanar distance of ~0.317 nm, which can be attributed to the (220) family planes and is in good agreement with the tetragonal lattice parameters calculated from PXRD data (d_{220} = 0.314 nm).

Physical Property and Optical Study of Single Crystal $MAPbI_3$ Nanostructures. We further used these single crystal nanostructures to characterize the fundamental physical properties of $MAPbI_3$. To determine whether the nanostructures are intrinsic or slightly doped n-type semiconductors, we studied the $MAPbI_3$ nanostructures (shown in Figure 2d) using time-resolved surface photoresponse (SPR) measurements, which is a contactless technique to reveal charge separation on the surface of a material.[50] The positive sign of the SPR signal (Figure S1a,b in the Supporting Information) indicates an accumulation of positive charges at the surface. For an n-type semiconductor, there is often upward band-bending near the surface, because most semiconductors have their surface Fermi levels pinned approximately near the middle of the bandgap.[51] This position causes an accumulation of holes near the surface upon exciting the semiconductors. Therefore, the sign of the signal observed in the SPR measurements confirms that these single crystal $MAPbI_3$ nanostructures are n-type semiconductors, which is similar to the n-type doping observed for the polycrystalline $MAPbI_3$ thin film (Figure S1c,d in the Supporting Information) synthesized following common procedures.[6]

Preliminary optical studies show that these single crystal $MAPbI_3$ nanostructures have better photophysical characteristics than the polycrystalline thin films commonly reported and bulk crystals grown from aqueous solutions. The nanoplates are transferred from FTO to silicon substrates coated with SiO_2 (330 nm) by the dry transfer method. The photoluminescence (PL) of the single objects is collected with a confocal Raman microscope using a 532 nm laser source. The onset of the $MAPbI_3$ film absorption spectrum (Figure 3d, black curve) occurs at ~790 nm, corresponding to a bandgap of 1.57 eV. The representative confocal PL spectrum of a single $MAPbI_3$ nanoplate (Figure 3d, blue curve) at room temperature shows a band-edge emission peak of 784 nm with a width at half-maximum of ~40 nm. The inset in Figure 3d shows a typical dark-field microscopy image of a single perovskite nanoplate. We also measured the PL of a bulk $MAPbI_3$ single crystal grown by slow precipitation from aqueous solution of hydroiodic acid containing lead precursor and methylammonium iodide (see Experimental Section for detail and Figure S2, Supporting Information, for photographs of such crystals) following a reported synthesis.[52] A much weaker PL (~200 times weaker intensity than that from nanoplate) was detected from the bulk crystal (Figure 3d, red curve). To better understand the photoexcited charge carrier dynamics, we further performed ultrafast pump−probe spectroscopy measurements on $MAPbI_3$ nanostructures and bulk single crystals. Figure 3e shows photoexcited carrier kinetics of both $MAPbI_3$ samples at a low pump fluence of 9.8 $\mu J/cm^2$. The $MAPbI_3$ nanostructures exhibit a carrier lifetime of 3.0 ns in a single exponential fit, while the bulk single crystal presents a much faster decay component with a lifetime of 0.47 ns after photoexcitation. The faster decay of photoexcited carriers and weaker PL in the bulk crystal is likely due to surface trap mediated nonradiative recombination.[9] Therefore, even though the crystal structure of the bulk and nanostructures is identical, we believe different preparation methods are the cause of higher (surface) defect density in bulk single crystals, which is likely due to the severe loss of MAI that is more soluble in water when the single crystals are taken from aqueous solutions. Furthermore, the carrier lifetime observed for these $MAPbI_3$ nanostructures is also longer than that reported for typical solution-processed polycrystalline thin films observed under similar pump fluence.[6,53,54] In conclusion, the stronger room-temperature PL and longer carrier lifetime observed in these as-grown single crystal $MAPbI_3$ nanostructures indicate superior optical and semiconducting quality.

Growth of Nanostructured $MAPbI_3$ Films for Photovoltaic Application. As presented above, single crystal $MAPbI_3$ NWs and nanoplates can be synthesized using MAI/IPA solutions within a concentration range of 20−50 mg/mL. However, when 10 mg/mL MAI/IPA solution was used, small cubic-like $MAPbI_3$ grains of a few hundred nanometers are formed on the surface (Figure 1b) and result in incomplete conversion. Surprisingly, we further found the morphology of the converted $MAPbI_3$ changed significantly as the MAI concentration decreased slightly below 10 mg/mL. $MAPbI_3$ films converted at 5, 7.5, and 10 mg/mL with a reaction time of

DOI: 10.1021/jacs.5b02651
J. Am. Chem. Soc. 2015, 137, 5810−5818

2 min are shown in Figure 4 and labeled as film A, film B, and film C, respectively. The A and B films are distinctly different.

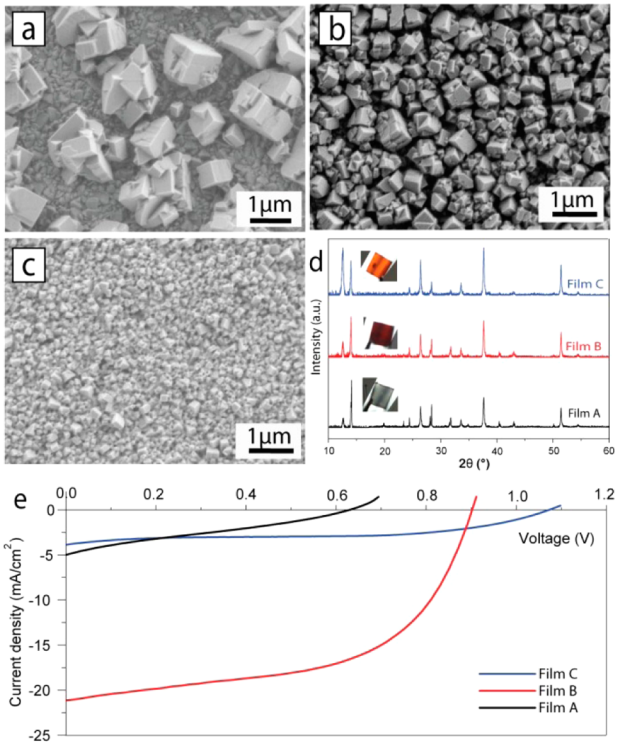

Figure 4. Structural characterizations and photovoltaic applications of nanostructured $MAPbI_3$ films converted at low MAI precursor concentrations. (a–c) SEM images of nanostructured $MAPbI_3$ films converted at MAI concentration of (a) 5 mg/mL, (b) 7.5 mg/mL, and (c) 10 mg/mL with a conversion time of 2 min. (d) The PXRD patterns of these as-converted $MAPbI_3$ films; insets are the corresponding optical images. (e) The current–voltage (J–V) curves of the solar cells fabricated from these nanostructured $MAPbI_3$ samples.

Film A has microsized (1–2 μm) "island-like" polycrystalline domains with a poor coverage on FTO (Figure 4a), while film B shows ~0.5–1 μm polycrystalline grains and almost full coverage on FTO (Figure 4b). Film C has very good coverage but much smaller domain size (Figure 4c) typical of perovskite thin film conversion. More SEM comparisons are provided in Figure S3 in the Supporting Information. The physical appearance of three films is also significantly different (see inset images in Figure 4d). The color of film C formed with 10 mg/mL of MAI/IPA became light brown immediately (within several seconds) as PbI_2 was immersed into the solution. However, the color was almost unchanged during the remaining time suggesting that further conversion was obstructed. However, the color for the converted film B with 7.5 mg/mL MAI concentration gradually turned from yellow to brown and then to red–black in ~90 s. For the 5 mg/mL MAI concentration, the sample (film A) gradually changed to black with progressive exposure of the underlying FTO substrate over ~60 s. The corresponding PXRD patterns (Figure 4d) show that all as-converted products are the perovskite phase, even though some PbI_2 remained. Also, film A and film B have better crystallinity than film C, as indicated by the split of (004) and (220) diffraction peaks near the 2θ of 28°.

Photovoltaic devices were then fabricated with these polycrystalline nanostructured $MAPbI_3$ films and investigated (see Experimental Section for details of device fabrication and measurement). Figure 4e shows the corresponding J–V curves, and the device parameters are tabulated in Table 1. Preliminary

Table 1. Photovoltaic Device Parameters of Perovskite Solar Cells Constructed with Nanostructured $MAPbI_3$ Film A, Film B, and Film C

device	V_{oc} (V)	J_{sc} (mA/cm^2)	FF	η (%)
film A	0.634	4.9	0.26	0.8
film B	0.900	21.0	0.55	10.6
film C	1.07	3.9	0.50	1.4

results show that film B had the best photovoltaic performance with a short-circuit current density (J_{sc}) of 21.0 mA/cm^2, an open-circuit voltage (V_{oc}) of 900 mV, a fill factor (FF) of 0.55, and a power conversion efficiency of 10.6%. The very poor performance of film A is likely due to the discontinuities caused by numerous pinholes in the film. The pinholes in $MAPbI_3$ film can cause serious recombination, resulting in a decrease in V_{oc} and J_{sc}.[55] Film C had a higher V_{oc} than film B, but the J_{sc} was much smaller. The higher V_{oc} can be explained by the full coverage, while the smaller J_{sc} is likely due to the less complete conversion into perovskite in film C. Moreover, film B showed much higher light absorption than film C, as shown in Figure S4 in the Supporting Information. Compared to the single crystal nanostructures in Figure 2d, the absorption spectra and PL spectra of these microsized crystals (film A and B) display a small blue shift in the absorption edge and PL peak (Figure S5a–c in the Supporting Information), which is in agreement with the finding that larger crystallites present smaller band gap reported by D'Innocenzo et al.[56] Moreover, film B showed similar carrier dynamics to the single crystal nanostructures (Figure S5d in the Supporting Information), suggesting "single crystal-like" properties in such microsized crystals films. Recently, Park and co-workers have also shown that similar microsized crystalline perovskite grains can enhance both light-harvesting efficiency and carrier extraction efficiency and achieved solar cells with efficiency as high as 17% after optimization.[19] However, we note that it is difficult to create microsized nanostructured $MAPbI_3$ films with full coverage consistently, because the morphology of such converted nanostructures is very sensitive to the MAI concentration and the morphology of the predeposited PbI_2 film. We believe that more refined control of crystal morphology and more optimization of the device fabrication can further improve the efficiency of solar devices based on these nanostructured perovskite thin films.

Growth Mechanisms of Crystalline $MAPbI_3$ Nanostructures. To explain these observed trends in the crystal growth of $MAPbI_3$ nanostructures, it is necessary to understand the underlying mechanisms of conversion. We propose that there are actually two growth mechanisms: a solid–liquid interfacial conversion reaction (Figure 5a) and a dissolution-recrystallization growth mechanism (Figure 5b). At low concentration (≤8 mg/mL) of MAI precursor, the conversion occurs by a solid–liquid interfacial reaction where the diffusion of the MAI into the layered structured PbI_2 results in the direct formation of $MAPbI_3$, following reaction a below. The interfacial reaction will be gradually suppressed as crystalline $MAPbI_3$ forms on the surface and obstructs further MA^+ diffusion into the underlying PbI_2. The obstruction could lead to the incomplete conversion seen in Figure 4a and b.

DOI: 10.1021/jacs.5b02651
J. Am. Chem. Soc. 2015, 137, 5810–5818

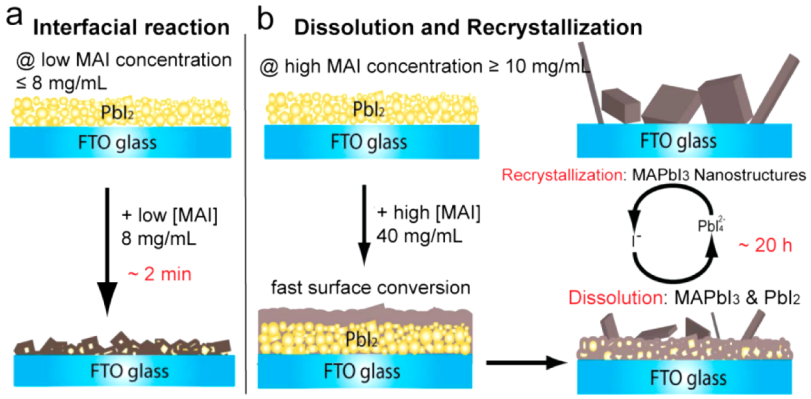

Figure 5. Schematic illustrations of the two growth mechanisms of crystalline $MAPbI_3$ nanostructures: (a) interfacial reaction mechanism at lower MAI concentration and (b) dissolution-recrystallization growth mechanism at higher MAI concentration. The conversion via interfacial reaction is faster than dissolution-recrystallization growth.

$$PbI_2(s) + CH_3NH_3^+(sol) + I^-(sol) \rightarrow CH_3NH_3PbI_3(s) \quad (a)$$

However, at higher MAI concentrations (≥10 mg/mL), crystalline $MAPbI_3$ thin film immediately forms on the PbI_2 surface and severely obstructs the diffusion of MA^+ and I^- ions and their reaction with PbI_2. This mechanism results in rather incomplete conversion after a short period of reaction as confirmed by PXRD (Figure 1i). However, further increases in MAI and thus I^- concentration (≥20 mg/mL) result in the thermodynamically favorable formation of PbI_4^{2-} complex ions in the solution. The fact that PbI_2 becomes more soluble in concentrated iodide solution due to the formation of lead iodide complex ions (PbI_4^{2-}) has been observed previously.[27,57−59] Such an excess amount of I^- ions can provide the driving force that dissolves the initially formed $MAPbI_3$ and the buried, unconverted PbI_2 by the following reactions until the local concentration of PbI_4^{2-} reach saturation:

$$CH_3NH_3PbI_3(s) + I^-(sol) \rightarrow CH_3NH_3^+(sol) + PbI_4^{2-}(sol) \quad (b)$$

$$PbI_2(s) + 2I^-(sol) \rightarrow PbI_4^{2-}(sol) \quad (c)$$

After the MAI solution is oversaturated with PbI_4^{2-} complexes, PbI_4^{2-} ions will react with $CH_3NH_3^+$ ions and slowly recrystallize to grow single crystal $MAPbI_3$ NWs and nanoplates (reaction d).

$$PbI_4^{2-}(sol) + CH_3NH_3^+(sol) \rightarrow CH_3NH_3PbI_3(s) + I^-(sol) \quad (d)$$

The proper local low supersaturation of crystal growth precursors and the slow release of precursor from the surface as controlled by reaction c could facilitate the anisotropic crystal growth and formation of 1D NWs, NRs, and 2D nanoplates.[29,60,61] However, if MAI concentration is too high (≥70 mg/mL), most PbI_2 precursor gets dissolved and exists as PbI_4^{2-} in the solution, and only very little can reprecipitate to form $MAPbI_3$ nanostructures (Figure 1h).

The growth behaviors observed when we used MABr to replace MAI precursor further confirmed the growth mechanisms discussed above. With a low MABr concentration of 4 mg/mL and a reaction time of 1 min, the PXRD (Figure 6a, black curve) shows diffraction peaks at 14.71°, 20.93°, and 29.80°, which can be assigned to the (100), (110), and (200)

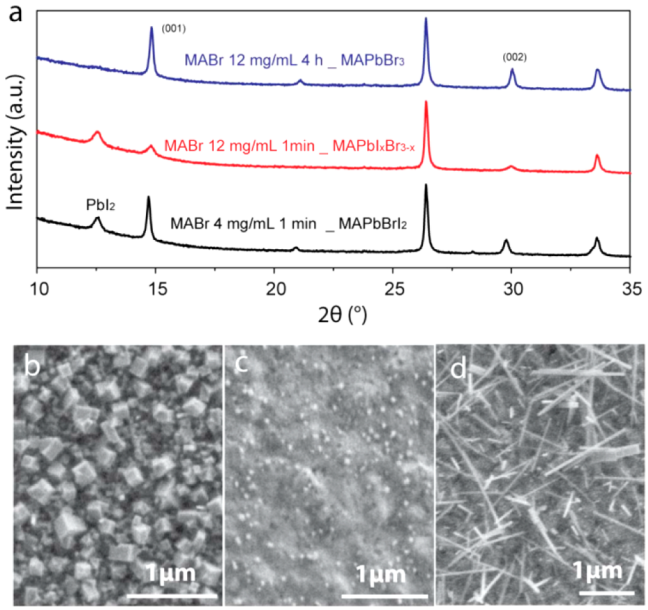

Figure 6. Structural characterizations of $MAPbI_2Br$, $MAPbI_xBr_{3-x}$, and $MAPbBr_3$ nanostructures synthesized using PbI_2 precursor and different concentrations of MABr/IPA solutions and reaction time. (a) PXRD patterns of these films. (b−d) SEM images of as-grown nanostructures at (b) MABr concentration of 4 mg/mL and reaction time of 1 min, (c) MABr concentration of 12 mg/mL and reaction time of 1 min, and (d) MABr concentration of 12 mg/mL and reaction time of 4 h.

lattice planes of $MAPbI_2Br$. The PL has a strong emission at 739 nm (Figure S6 in the Supporting Information) that is characteristic of the $MAPbI_2Br$ phase.[9] SEM of the as-converted film revealed cubic-like polycrystalline grains (Figure 6b) similar to Figure 4b. The formation of mixed halide $MAPbI_2Br$ confirms that the direct interfacial conversion reaction mechanism dominates at a low MABr or MAI precursor concentration.

$$PbI_2(s) + CH_3NH_3^+(sol) + Br^-(sol) \rightarrow CH_3NH_3PbI_2Br(s) \quad (e)$$

However, when the MABr concentration is 12 mg/mL and the reaction time is 1 min, the PXRD (Figure 6a, red curve) shows that the (100) and (200) diffraction peaks shift to higher

DOI: 10.1021/jacs.5b02651
J. Am. Chem. Soc. 2015, 137, 5810−5818

angles 14.81° and 29.96°, respectively, indicating the as-converted film becomes $MAPbI_xBr_{3-x}$. However, there is still unconverted PbI_2 in the film. The corresponding SEM shows that a compact layer of $MAPbI_xBr_{3-x}$ is formed on the surface with many points of nucleation (Figure 6c). When the reaction time is further increased to 4 h, the PXRD shows diffraction peaks at 14.83°, 21.12°, and 30.04° corresponding to the (100), (110), and (200) lattice planes of the *cubic* $MAPbBr_3$ phase (space group $Pm\bar{3}m$, a = 5.9334 Å) and the diffraction peak from PbI_2 disappears. SEM shows NWs (of single crystal $MAPbBr_3$) are grown on the surface (Figure 6d). These $MAPbBr_3$ NWs are ~2 μm in length and ~100 nm in diameter. These $MAPbBr_3$ NWs also show very strong PL at room temperature (Figure S6 in the Supporting Information). The high concentrations of Br^- ions from MABr precursor can result in the dissolution of PbI_2 to form $PbBr_4^{2-}$ complexes due to the overwhelming excess of Br^- ions in reaction f, and thus enable the growth of pure $MAPbBr_3$ NWs after they recrystallize with the $CH_3NH_3^+$ ions following reaction g. These results are in agreement with the dissolution-recrystallization growth mechanism.

$$PbI_2(s) + 4Br^-(sol) \rightarrow PbBr_4^{2-}(sol) + 2I^-(sol) \quad (f)$$

$$PbBr_4^{2-}(sol) + CH_3NH_3^+(sol) \rightarrow CH_3NH_3PbBr_3(s) + Br^-(sol) \quad (g)$$

Following the dissolution-recrystallization growth mechanism, we further realized that the lead precursor does not have to be limited to PbI_2 to grow $MAPbI_3$ NWs and nanoplates. Therefore, we replaced the PbI_2 with lead acetate trihydrate ($PbAc_2{\cdot}3H_2O$) and, as expected, we were still able to synthesize single crystal $MAPbI_3$ nanostructures (see Figure S7 in the Supporting Information). The lead acetate was deposited on the FTO substrate by spin-coating a lead acetate trihydrate aqueous solution. Because of the partial hydrolysis of lead acetate, the resulting film is actually $3PbAc_2{\cdot}PbO{\cdot}H_2O$ as revealed by PXRD (Figure S6d in the Supporting Information, red curve, PDF19-1789). Despite that minor detail, it is very clear that $MAPbI_3$ NWs and nanoplates can be readily grown at the 40 mg/mL MAI/IPA solution concentration and a 1 h reaction time. The PXRD (Figure S6d in the Supporting Information, blue curve) confirms that the as-grown product is the pure tetragonal phase $MAPbI_3$. Interestingly, we find that this approach also leads to a faster growth of $MAPbI_3$ than when PbI_2 is used as the precursor. The length of the NWs can reach 6 μm in 1 h reaction time, almost triple that of the NWs in Figure 2b, which were grown for the same amount of time. The size of nanoplates is also much larger. The faster growth may occur because $PbAc_2$ is much more soluble than PbI_2, and thus PbI_4^{2-} complexes are formed and become saturated for crystal growth more quickly. These results further support the dissolution-recrystallization growth pathway proposed for the $MAPbI_3$ nanostructure growth.

CONCLUSION

In conclusion, we have demonstrated the synthesis of single crystal $MAPbI_3$ nanowires, nanorods, and nanoplates via a dissolution-recrystallization growth mechanism in the solution conversion from PbI_2 (and $PbAc_2$) to $MAPbI_3$. PXRD and TEM confirm the good single crystal quality and tetragonal perovskite phase of these nanostructures. These single crystal nanostructures are identified as *n*-type semiconductors by surface photovoltage measurement. Moreover, these nanostructures have stronger room-temperature photoluminescence and longer excited state lifetimes than their bulk and thin film counterparts. These single-crystal nanostructures not only can serve as model systems for studying the fundamental electrical transport and optical properties of $MAPbI_3$ and improving them for solar energy conversion applications but also can be interesting building blocks for nanophotonic/electronic applications,[35,41] for example, nanowire lasers.[62] On the basis of the new understanding of the two different growth mechanisms of $MAPbI_3$, we have also created a highly crystalline nanostructured $MAPbI_3$ film with micrometer grain size and high surface coverage via an interfacial reaction and demonstrated solar cell devices with a good 10.6% photovoltaic efficiency based on such a film. These results provide new insights into the crystal growth of $MAPbI_3$ that are important for the further development of improved photovoltaic and optoelectronic devices based on these new classes of organic−inorganic lead halide perovskite semiconductors.

EXPERIMENTAL SECTION

All chemicals and regents were purchased from Sigma-Aldrich and used as received unless noted otherwise.

Synthesis of CH_3NH_3I and CH_3NH_3Br. The CH_3NH_3I (MAI) was synthesized by slowly mixing 1:1 methylamine (40% in methanol) and HI (57 wt % in water) in a flask. The CH_3NH_3I salt precipitated as the solvent was carefully evaporated. The product was washed with diethyl ether several times and then dried at 80 °C in a vacuum oven for ~24 h. The CH_3NH_3Br (MABr) was synthesized using a similar method using HBr.

Growth of $MAPbI_3$ and $MAPbBr_3$ Nanostructures. The single crystal $MAPbI_3$ nanostructures were synthesized by placing lead iodide (PbI_2) or lead acetate ($PbAc_2$) film on fluorine-doped tin oxide-coated glass substrates (FTO, 10 Ω/sq) or glass slides (for optical characterization) into a MAI solution in isopropanol (1 mL), with the lead precursor-coated side facing up at room temperature (22 °C). For the synthesis of $MAPbBr_3$ nanostructures, the substrate was placed in MABr solution in isopropanol (1 mL), with the PbI_2-coated side facing down. The PbI_2 film was prepared by spin-coating a solution of 400 mg/mL PbI_2 (99.99%) in dimethylformamide (DMF) at 3000 rpm for 15 s. The $PbAc_2$ film was prepared by spin-coating a solution of 100 mg/mL $PbAc_2{\cdot}3H_2O$ in nanopure water at 2000 rpm for 30 s. Before spin-coating, the FTO substrate was ultrasonically cleaned in IPA, acetone, and ethanol for 5 min sequentially and then was cleaned with oxygen plasma (150 W RF, 1 sccm O_2, < 200 mTorr, 3 min) to remove organic residues. Both PbI_2 and $PbAc_2$ film were dried at 100 °C for 30 s to remove the remnant solvent before being placed into the MAI solution. After a specified reaction time, the FTO substrate was removed and dipped into isopropanol solvent to remove any leftover salt on the film, dried under a stream of nitrogen flow, and then dried on a hot plate at 100 °C for another 15 s.

Synthesis of Bulk $MAPbI_3$ Single Crystals. Following the previously reported method,[52] the $MAPbI_3$ single crystals were grown by slow precipitation from a hydroiodic acid solution containing lead precursor. Specify, 2.9 g of $PbAc_2{\cdot}3H_2O$ was dissolved in 10 mL of a concentrated aqueous HI solution (57 wt %) in a 100 mL flask and heated to 100 °C in an oil bath. After 3.1 g of CH_3NH_3I was added to this solution, a lot of precipitate was formed by slowly cooling the solution from 100 to 40 °C in 60 h. These products were collected and rinsed with IPA several times before being dried on a hot plate.

Structural Characterizations of Perovskite Nanostructures. The scanning electron microscopy was performed using a LEO SUPRA 55 VP field-emission SEM operated at 1.5 kV. The sample for transmission electron microscopy was prepared by dry-transferring the as-grown $MAPbI_3$ nanostructures onto a TEM grid (Ted Pella, lacey carbon type-A support film, 300-mesh, copper, no. 01890-F). The transmission electron microscopy was carried out on a FEI Titan

DOI: 10.1021/jacs.5b02651
J. Am. Chem. Soc. 2015, 137, 5810−5818

scanning transmission electron microscope (STEM) at an accelerating voltage of 200 kV or Technai T12 TEM at an accelerating voltage of 120 kV. The PXRD data were collected on as as-grown samples on substrates using a Bruker D8 Advance Powder X-ray diffractometer with Cu Kα radiation. The background was fitted and then subtracted using Jade program.

Surface Photoresponse Measurement. The sample used in time-resolved SPR was synthesized using PbI_2 precursor and 40 mg/mL of MAI/IPA solution at a reaction time of 20 h. The measurements were performed under ambient conditions (in air) in a capacitor-like arrangement. The perovskite sample and an FTO/glass electrode were assembled in a custom-made cell holder separated by a 127 μm thick Teflon spacer. The sample was illuminated through the FTO sense electrode by ~3 ns pulses at 0.1 mJ/pulse from a tunable laser (NT340, Ekspla, Inc., Vilnius, Lithuania). The signal collected was using exciting wavelength at 700 nm. The response from the sense electrode was amplified by a fast amplifier (model TA2000B-1, FAST ComTec GmbH, Oberhaching/München, Germany) with 50 Ω input and output impedances, 1.5 GHz bandwidth, and 10× voltage gain, and was recorded by a digital oscilloscope (DSO9404A, Agilent, Inc., Santa Clara, CA).

Optical Characterization of $MAPbI_3$ Nanostructures and Bulk Crystals. The photoluminescence (PL) of single crystal nanoplates and bulk crystals was collected with an Aramis Confocal Raman microscope using a 532 nm laser source with a neutral density filter D4 and D3, respectively. The spatial resolution was ~1 μm. The samples for PL measurement and dark-field image were transferred from FTO substrates to silicon substrates covered with SiO_2 (330 nm) by a dry-transfer method. The dark field image of nanoplate (Figure 3d inset) was taken using an optical microscope (Olympus, BX51M). The UV−vis absorption of as-grown thin film was collected using a JASCO V-550 spectrometer.

For ultrafast pump−probe spectroscopy, the $MAPbI_3$ nanostructures were sealed with two pieces of glass slides using parafilm as a spacer on a hot plate (100 °C) to minimize the exposure to moisture in the air. The pump beam was at 600 nm with a full width at half maximum (fwhm) diameter at sample position, which was measured to be 1.44 mm, and pump power was set at 9.8 $\mu J/cm^2$. The probe was set at 795 nm with a fwhm diameter of 589 μm. Both pulses had 50 fs fwhm, and the pump beam was chopped to half the repetition rate of the probe to allow active background subtraction. Transient absorption mode was used for the nanostructures, and transient reflection mode was used for bulk single crystals. Both were measured from −200 ps to 3.7 ns in 50 ps steps.

Fabrication and Characterization of Solar Cells. The FTO substrate was first patterned by etching with a 2 M HCl solution and Zn powders around a mask formed by strips of adhesive tape (3M, Scotch Magic tape). Before spin-coating PbI_2, a layer of compact TiO_2 film was deposited by spin-coating a solution that consisted of 0.23 M titanium isopropoxide and 0.013 M HCl solution in isopropanol at 2000 rpm for 60 s on such a patterned FTO substrate. This Ti precursor solution was prepared according to previous literature reports.[63] The FTO substrate was then annealed in a muffle furnace at 500 °C for 30 min. The procedures of PbI_2 deposition and its conversion to nanostructured $MAPbI_3$ film followed the procedures presented previously. After $MAPbI_3$ conversion, a hole conductor layer was deposited on nanostructured $MAPbI_3$ films by spin-coating a solution containing 70 mg of spiro-MeOTAD, 30 μL of 4-*tert*-butylpyridine, and 18 μL of 520 mg/mL acetonitrile solution of lithium bis(trifluoromethylsulfonyl)imide in 1 mL of chlorobenzene at 3000 rpm for 30 s. The Au counterelectrode was deposited on spiro-MeOTAD film by e-beam evaporating 100 nm of Au (Kurt J. Lesker Co., 99.99%) at 1 Å/s. A 1 kW Xe short arc lamp solar simulator (Newport Corp., model 91191) with a AM1.5G filter was used to illuminate the devices at an intensity of 100 mW/cm^2. All $J-V$ curve measurements were recorded in a two-electrode configuration using a Bio-Logic SP-200 potentiostat at a scan rate of 100 mV/s. The area of the device was defined by the overlap of Au contact and FTO electrode, which was ~0.08 cm^2. The accurate value was measured by reading pixels of micrographs taken with an optical microscope.

■ ASSOCIATED CONTENT

Supporting Information

Addition SEM images, PXRD patterns, optical characterization, and surface photoresponse measurements of various products. This material is available free of charge via the Internet at http://pubs.acs.org.

■ AUTHOR INFORMATION

Corresponding Author

*jin@chem.wisc.edu

Notes

The authors declare no competing financial interest.

■ ACKNOWLEDGMENTS

This research is supported by the U.S. Department of Energy, Office of Basic Energy Sciences, Division of Materials Sciences and Engineering, under Award DE-FG02-09ER46664. D.M. thanks the China Scholarship Council (CSC) for support.

■ REFERENCES

(1) Kim, H. S.; Lee, C. R.; Im, J. H.; Lee, K. B.; Moehl, T.; Marchioro, A.; Moon, S. J.; Humphry-Baker, R.; Yum, J. H.; Moser, J. E.; Gratzel, M.; Park, N. G. *Sci. Rep.* **2012**, *2*, 591.

(2) Lee, M. M.; Teuscher, J.; Miyasaka, T.; Murakami, T. N.; Snaith, H. J. *Science* **2012**, *338*, 643.

(3) Burschka, J.; Pellet, N.; Moon, S. J.; Humphry-Baker, R.; Gao, P.; Nazeeruddin, M. K.; Gratzel, M. *Nature* **2013**, *499*, 316.

(4) Liu, M. Z.; Johnston, M. B.; Snaith, H. J. *Nature* **2013**, *501*, 395.

(5) Stranks, S. D.; Eperon, G. E.; Grancini, G.; Menelaou, C.; Alcocer, M. J. P.; Leijtens, T.; Herz, L. M.; Petrozza, A.; Snaith, H. J. *Science* **2013**, *342*, 341.

(6) Xing, G. C.; Mathews, N.; Sun, S. Y.; Lim, S. S.; Lam, Y. M.; Gratzel, M.; Mhaisalkar, S.; Sum, T. C. *Science* **2013**, *342*, 344.

(7) Green, M. A.; Ho-Baillie, A.; Snaith, H. J. *Nat. Photonics* **2014**, *8*, 506.

(8) Tan, Z. K.; Moghaddam, R. S.; Lai, M. L.; Docampo, P.; Higler, R.; Deschler, F.; Price, M.; Sadhanala, A.; Pazos, L. M.; Credgington, D.; Hanusch, F.; Bein, T.; Snaith, H. J.; Friend, R. H. *Nat. Nanotechnol.* **2014**, *9*, 687.

(9) Xing, G. C.; Mathews, N.; Lim, S. S.; Yantara, N.; Liu, X. F.; Sabba, D.; Gratzel, M.; Mhaisalkar, S.; Sum, T. C. *Nat. Mater.* **2014**, *13*, 476.

(10) Deschler, F.; Price, M.; Pathak, S.; Klintberg, L. E.; Jarausch, D. D.; Higler, R.; Huttner, S.; Leijtens, T.; Stranks, S. D.; Snaith, H. J.; Atature, M.; Phillips, R. T.; Friend, R. H. *J. Phys. Chem. Lett.* **2014**, *5*, 1421.

(11) Zhou, H. P.; Chen, Q.; Li, G.; Luo, S.; Song, T. B.; Duan, H. S.; Hong, Z. R.; You, J. B.; Liu, Y. S.; Yang, Y. *Science* **2014**, *345*, 542.

(12) Jeon, N. J.; Noh, J. H.; Kim, Y. C.; Yang, W. S.; Ryu, S.; Seok, S. I. *Nat. Mater.* **2014**, *13*, 897.

(13) Snaith, H. J. *J. Phys. Chem. Lett.* **2013**, *4*, 3623.

(14) Ball, J. M.; Lee, M. M.; Hey, A.; Snaith, H. J. *Energy Environ. Sci.* **2013**, *6*, 1739.

(15) Liu, D. Y.; Kelly, T. L. *Nat. Photonics* **2014**, *8*, 133.

(16) Malinkiewicz, O.; Yella, A.; Lee, Y. H.; Espallargas, G. M.; Graetzel, M.; Nazeeruddin, M. K.; Bolink, H. J. *Nat. Photonics* **2014**, *8*, 128.

(17) Chen, Q.; Zhou, H. P.; Hong, Z. R.; Luo, S.; Duan, H. S.; Wang, H. H.; Liu, Y. S.; Li, G.; Yang, Y. *J. Am. Chem. Soc.* **2014**, *136*, 622.

(18) Crossland, E. J. W.; Noel, N.; Sivaram, V.; Leijtens, T.; Alexander-Webber, J. A.; Snaith, H. J. *Nature* **2013**, *495*, 215.

(19) Im, J. H.; Jang, I. H.; Pellet, N.; Gratzel, M.; Park, N. G. *Nat. Nanotechnol.* **2014**, *9*, 927.

(20) Abate, A.; Saliba, M.; Hollman, D. J.; Stranks, S. D.; Wojciechowski, K.; Avolio, R.; Grancini, G.; Petrozza, A.; Snaith, H. J. *Nano Lett.* **2014**, *14*, 3247.

DOI: 10.1021/jacs.5b02651
J. Am. Chem. Soc. 2015, 137, 5810−5818

(21) Noel, N. K.; Abate, A.; Stranks, S. D.; Parrott, E. S.; Burlakov, V. M.; Goriely, A.; Snaith, H. J. *ACS Nano* **2014**, *8*, 9815.
(22) Nie, W.; Tsai, H.; Asadpour, R.; Blancon, J. C.; Neukirch, A. J.; Gupta, G.; Crochet, J. J.; Chhowalla, M.; Tretiak, S.; Alam, M. A.; Wang, H. L.; Mohite, A. D. *Science* **2015**, *347*, 522.
(23) Dong, Q.; Fang, Y.; Shao, Y.; Mulligan, P.; Qiu, J.; Cao, L.; Huang, J. *Science* **2015**, *347*, 967.
(24) Shi, D.; Adinolfi, V.; Comin, R.; Yuan, M.; Alarousu, E.; Buin, A.; Chen, Y.; Hoogland, S.; Rothenberger, A.; Katsiev, K.; Losovyj, Y.; Zhang, X.; Dowben, P. A.; Mohammed, O. F.; Sargent, E. H.; Bakr, O. M. *Science* **2015**, *347*, 519.
(25) Moore, D. T.; Sai, H.; Tan, K. W.; Smilgies, D. M.; Zhang, W.; Snaith, H. J.; Wiesner, U.; Estroff, L. A. *J. Am. Chem. Soc.* **2015**, *137*, 2350.
(26) Hao, F.; Stoumpos, C. C.; Liu, Z.; Chang, R. P. H.; Kanatzidis, M. G. *J. Am. Chem. Soc.* **2014**, *136*, 16411.
(27) Yang, S.; Zheng, Y.; Hou, Y.; Chen, X.; Chen, Y.; Wang, Y.; Zhao, H.; Yang, H. G. *Chem. Mater.* **2014**, *26*, 6705−6710.
(28) Dasgupta, N. P.; Sun, J.; Liu, C.; Brittman, S.; Andrews, S. C.; Lim, J.; Gao, H.; Yan, R.; Yang, P. *Adv. Mater.* **2014**, *26*, 2137.
(29) Meng, F.; Morin, S. A.; Forticaux, A.; Jin, S. *Acc. Chem. Res.* **2013**, *46*, 1616.
(30) Kelzenberg, M. D.; Boettcher, S. W.; Petykiewicz, J. A.; Turner-Evans, D. B.; Putnam, M. C.; Warren, E. L.; Spurgeon, J. M.; Briggs, R. M.; Lewis, N. S.; Atwater, H. A. *Nat. Mater.* **2010**, *9*, 368.
(31) Kim, S. K.; Day, R. W.; Cahoon, J. F.; Kempa, T. J.; Song, K. D.; Park, H. G.; Lieber, C. M. *Nano Lett.* **2012**, *12*, 4971.
(32) Huang, M. H.; Mao, S.; Feick, H.; Yan, H. Q.; Wu, Y. Y.; Kind, H.; Weber, E.; Russo, R.; Yang, P. D. *Science* **2001**, *292*, 1897.
(33) Tang, J. Y.; Huo, Z. Y.; Brittman, S.; Gao, H. W.; Yang, P. D. *Nat. Nanotechnol.* **2011**, *6*, 568.
(34) Lu, W.; Lieber, C. M. *Nat. Mater.* **2007**, *6*, 841.
(35) Yan, R. X.; Gargas, D.; Yang, P. D. *Nat. Photonics* **2009**, *3*, 569.
(36) Caban-Acevedo, M.; Liang, D.; Chew, K. S.; DeGrave, J. P.; Kaiser, N. S.; Jin, S. *ACS Nano* **2013**, *7*, 1731.
(37) Tian, B.; Kempa, T. J.; Lieber, C. M. *Chem. Soc. Rev.* **2009**, *38*, 16.
(38) Liang, D.; Caban-Acevedo, M.; Kaiser, N. S.; Jin, S. *Nano Lett.* **2014**, *14*, 6754.
(39) Kempa, T. J.; Day, R. W.; Kim, S. K.; Park, H. G.; Lieber, C. M. *Energy Environ. Sci.* **2013**, *6*, 719.
(40) Ha, S. T.; X.F, L.; Zhang, Q.; Giovanni, D.; Sum, T. C.; Xiong, Q. H. *Adv. Opt. Mater.* **2014**, *2*, 838.
(41) Zhang, Q.; Ha, S. T.; Liu, X.; Sum, T. C.; Xiong, Q. *Nano Lett.* **2014**, *14*, 5995.
(42) Im, J. H.; Luo, J.; Franckevicius, M.; Pellet, N.; Gao, P.; Moehl, T.; Zakeeruddin, S. M.; Nazeeruddin, M. K.; Gratzel, M.; Park, N. G. *Nano Lett.* **2015**, *15*, 2120.
(43) Zhuo, S.; Zhang, J.; Shi, Y.; Huang, Y.; Zhang, B. *Angew. Chem., Int. Ed.* **2015**, DOI: 10.1002/anie.201411956.
(44) Chen, Z.; Li, H.; Tang, Y.; Huang, X.; Ho, D.; Lee, S. *Mater. Res. Express* **2014**, *1*, 015034.
(45) Zhu, F.; Men, L.; Guo, Y.; Zhu, Q.; Bhattacharjee, U.; Goodwin, P. M.; Petrich, J. W.; Smith, E. A.; Vela, J. *ACS Nano* **2015**, *9*, 2948.
(46) Liang, K. N.; Mitzi, D. B.; Prikas, M. T. *Chem. Mater.* **1998**, *10*, 403.
(47) Baikie, T.; Fang, Y. N.; Kadro, J. M.; Schreyer, M.; Wei, F. X.; Mhaisalkar, S. G.; Graetzel, M.; White, T. J. *J. Mater. Chem. A* **2013**, *1*, 5628.
(48) Stoumpos, C. C.; Malliakas, C. D.; Kanatzidis, M. G. *Inorg. Chem.* **2013**, *52*, 9019.
(49) Kawamura, Y.; Mashiyama, H.; Hasebe, K. *J. Phys. Soc. Jpn.* **2002**, *71*, 1694.
(50) Benson, M. C.; Ruther, R. E.; Gerken, J. B.; Rigsby, M. L.; Bishop, L. M.; Tan, Y. Z.; Stahl, S. S.; Hamers, R. J. *ACS Appl. Mater. Interfaces* **2011**, *3*, 3110.
(51) Li, L. S.; Yu, Y. H.; Meng, F.; Tan, Y. Z.; Hamers, R. J.; Jin, S. *Nano Lett.* **2012**, *12*, 724.
(52) Poglitsch, A.; Weber, D. *J. Chem. Phys.* **1987**, *87*, 6373.
(53) Yamada, Y.; Nakamura, T.; Endo, M.; Wakamiya, A.; Kanemitsu, Y. *J. Am. Chem. Soc.* **2014**, *136*, 11610.
(54) Manser, J. S.; Kamat, P. V. *Nat. Photonics* **2014**, *8*, 737.
(55) Eperon, G. E.; Burlakov, V. M.; Docampo, P.; Goriely, A.; Snaith, H. J. *Adv. Funct. Mater.* **2014**, *24*, 151.
(56) D'Innocenzo, V.; Srimath Kandada, A. R.; De Bastiani, M.; Gandini, M.; Petrozza, A. *J. Am. Chem. Soc.* **2014**, *136*, 17730.
(57) Lanford, O. E.; Kiehl, S. J. *J. Am. Chem. Soc.* **1941**, *63*, 667.
(58) Clever, H. L.; Johnston, F. J. *J. Phys. Chem. Ref. Data* **1980**, *9*, 751−784.
(59) Horváth, O.; Mikó, I. *J. Photochem. Photobiol., A* **1998**, *114*, 95.
(60) Morin, S. A.; Bierman, M. J.; Tong, J.; Jin, S. *Science* **2010**, *328*, 476.
(61) Morin, S. A.; Forticaux, A.; Bierman, M. J.; Jin, S. *Nano Lett.* **2011**, *11*, 4449.
(62) Zhu, H.; Fu, Y.; Meng, F.; Wu, X.; Gong, Z.; Ding, Q.; Gustafsson, M. V.; Trinh, M. T.; Jin, S.; Zhu, X.-Y. *Nat. Mater.* **2015**, DOI: 10.1038/NMAT4271.
(63) Docampo, P.; Ball, J. M.; Darwich, M.; Eperon, G. E.; Snaith, H. J. *Nat. Commun.* **2013**, *4*, 2761.

DOI: 10.1021/jacs.5b02651
J. Am. Chem. Soc. 2015, 137, 5810−5818